RSC Advances

PAPER

View Article Online
View Journal | View Issue

Cite this: *RSC Adv.*, 2026, **16**, 23937

Graphene field-effect transistor based multiplexed sensing platform for simultaneous detection of multiple Alzheimer's disease biomarkers

Biyu Guo,[ab] Jiangyang Wang,[a] Feige Lou,[a] Baowei Yuan,[a] Zhibo Chen,[a] Chengjie Tang,[a] Weiao Chen,[a] Fangxuan Yi,[a] Jingjing Jiang,*[c] Guangxi Hu,[a] Chunxiao Cong [a] and Ye Lu *[a]

Received 29th September 2025
Accepted 26th February 2026

DOI: 10.1039/d5ra07384g

rsc.li/rsc-advances

Simultaneous detection of multiple biomarkers for one disease using a single drop of body fluid is challenging yet critical to confirm symptoms in the early stage. This study presents the development of a graphene field-effect transistor (GFET)-based multiplexed sensing platform designed for overcoming this obstacle. The platform utilizes a hexamethyldisilazane (HMDS) blocking layer as a hydrophobic treatment to enable recognition element (probe/aptamer) modifications within a small chip area (3 × 3 mm^2), and this further enables simultaneous detection of multiple targets (multi-targets) in complex biological samples. The optimized aptamer/probe functionalization also enhances the specificity, sensitivity, and accuracy of the sensor. The technology was demonstrated with Alzheimer's disease (AD) biomarkers as a case study. Two distinctive biomarkers, hsa-miR-125b and Aβ42, are detected simultaneously with distinguishable signatures, and the lowest tested concentration is 1 fM. The cross-check experiments also show the effectiveness of the multi-target detection capability. This concise platform paves the way for accurate detection of early-stage diseases when the simultaneous identification of multiple biomarkers is required.

Introduction

In the early-stage diagnosis of diseases, simultaneous detection of multiple biomarkers has become an emerging research focus. This is because the measurement of a single biomarker often fails to provide sufficient information to meet the requirements of accurate diagnosis for complex diseases.[1–3] Taking Alzheimer's disease (AD) as an example, the early-stage diagnostic accuracies of individual biomarkers such as hsa-miR-125b and Aβ42 are 76.5% (ref. 4 and 5) and 85%,[6,7] respectively. Detection of a single biomarker of these types of diseases may result in misleading or incorrect early-stage diagnoses, and subsequently delayed or ineffective medical treatment. Therefore, simultaneous detection of multiple biomarkers is required to improve diagnostic accuracy and reliability.[1] However, multi-target detection is still currently facing a series of technical challenges. Conventionally it often requires the use of different instruments and reagents for detecting each biomarker. For instance, hsa-miR-125b is typically detected using real-time quantitative PCR (qPCR)[5,8] or fluorescence *in situ* hybridization,[9] while Aβ42 is commonly detected by methods such as magnetic resonance imaging (MRI),[10] mass spectrometry (MS),[11] enzyme-linked immunosorbent assay (ELISA)[12] and so on.[13–16] These multi-platform and multi-step strategies increase procedural complexity and turn-around time. Unlike conventional workflows in which nucleic-acid and protein biomarkers are assayed on different platforms using separate aliquots—leading to cumulative sample consumption,[17–19] our HMDS-assisted multiplexed GFET array simultaneously detects both classes from a single small droplet on one chip. Therefore, the development of miniaturized and integrated high-performance sensor platforms capable of simultaneously detecting multiple biomarkers in a single drop of body fluid is desired.

In recent years, with the rapid advancement of micro-nanofabrication technology and research on two-dimensional materials, graphene field-effect transistor (GFET)-based biosensors have emerged for biomarker detection due to their high sensitivity, low detection limit, and excellent electrical performance.[20–24] However, despite the significant progress made in single-target detection using GFET-based biosensors, multi-target detection in such system has not been fully realized and multiple technical challenges remain. For instance, achieving precise spatial separation of multiple recognition elements (aptamer/probe) within a limited chip area is

[a]*State Key Laboratory of Integrated Chips and Systems, School of Information Science and Technology, Fudan University, Shanghai 200433, China. E-mail: lu_ye@fudan.edu.cn*

[b]*Lingang Laboratory, Shanghai 200031, China*

[c]*Department of Endocrinology and Metabolism, Zhongshan Hospital, Fudan University, Shanghai 200032, China. E-mail: jiang.jingjing@zs-hospital.sh.cn*

particularly critical to minimize cross-interference during the functionalization process. Furthermore, the sensitivity and stability of the sensor may be compromised when detecting multiple targets simultaneously. Finally, environmental interference and the challenges in complex data processing may also impact the accuracy and reliability of multi-target detection. These issues significantly undermine the capability of existing GFET sensors in multi-target detection.

In this study, we propose a GFET-based multi-functional sensing platform capable of achieving highly sensitive and specific detection of multiple biomarkers within a single droplet of body fluid. We introduce a surface treatment method that utilized hexamethyldisilazane (HMDS) to hydrophobically modify the blocking layer on the chip surface, enabling precise separation of functional regions. This effectively resolves issues such as non-specific binding and interference during the functionalization process of multiple recognition elements in a limited chip area. It is demonstrated multiple distinct recognition elements can be functionalized within a chip area within 3 mm × 3 mm without any interference. Through this approach, even in the presence of mixed target molecules, each recognition element could still specifically bind to its corresponding target molecule, indicating the potential of this method for multi-target detection. As a demonstration, we utilized two Alzheimer's disease biomarkers, hsa-miR-125b and Aβ42, mixed in an experimental solution for validation. The results confirmed that the platform was not only capable of simultaneously detecting these two biomarkers in mixed samples but also exhibited exceptional detection sensitivity, with a detection capability ranging from 1 fM to 100 pM. This demonstrates that the GFET-based multi-functional sensing platform provides a solution for multi-target detection particularly suitable for early-stage disease diagnosis. Furthermore, compared to the detection range of 1 ng ml^{-1} to 1 pg ml^{-1} for Aβ42 reported in the literature,[25] the proposed platform is capable of detecting at significantly lower concentration levels. The platform's high versatility also making it a potential powerful tool for advancing precise point of care medicine.

Experimental

A. Experimental materials

The monolayer graphene was purchased from ACS Material. Aβ42 and Aβ40 peptides, hsa-miR-125b RNA sequence, the hsa-miR-125b complementary DNA probe and the Aβ42 DNA aptamer were synthesized by Sangon Biotech (Shanghai) Co., Ltd. The peptides were purified by high-performance liquid chromatography (HPLC) to a purity of 95.339%, and their sequence accuracy was confirmed using electrospray ionization mass spectrometry (ESI-MS). The miRNA was synthesized as a single strand and purified by HPLC. The recognition elements used in this study comprised: (i) the hsa-miR-125b DNA probe, designed as the reverse-complement of the mature miRNA sequence,[25] and (ii) the Aβ42 DNA aptamer with a reported sequence from the literature;[26] both carried a 5′-amine modification. The recognition-element sequences and synthesized sample sequences are provided in Tables 1 and 2. Phosphate-buffered saline (PBS, pH 7.4) was purchased from BBI Life Sciences. Prior to electrical testing, the synthesized powders were dissolved in 1× PBS and diluted to the required concentration.

B. Multi-target GFET biosensor fabrication

The preparation of GFET devices involves three main steps: deposition of metal electrodes, graphene transfer, and patterning of the channel region with subsequent removal of residual materials. First, photolithography and electron beam evaporation techniques were employed to deposit 5 nm Ti and 50 nm Pt as the metal electrodes on a 4-inch Si/SiO_2 wafer. The metal electrodes were divided into four regions, with four source-drain electrode pairs configured in each region. The graphene channel was positioned between the source-drain electrodes, ensuring that each region contained four GFET devices. Next, the graphene was transferred to the surface of each device using a wet-transfer method, and the graphene channels were patterned by photolithography to achieve the desired position and size.

C. Hydrophobic layer treatment on device surface

The layout design for the deposition of hydrophobic material regions was optimized according to the device layout, with each chip consisting of 16 GFETs. A supporting layer of polymethyl methacrylate (PMMA, 950A4, Micro Chem Corp.) was first spin-coated to protect the graphene channel, followed by spin-coating of photoresist AZ5214 (Resemi) and annealing at 95 ° C for 2 minutes. The predefined patterns between the transistor devices were then exposed and developed. Next, 30 nm SiO_2 was deposited *via* electron beam evaporation, and the SiO_2 layer on the device surface was treated with HMDS to induce hydrophobicity. Since SiO_2 deposited by electron beam evaporation forms a significant number of polar hydroxyl (–OH) groups on its surface when exposed to air, making the substrate highly hydrophilic, a layer of non-polar HMDS molecules was chemically attached to the device surface. After heating, HMDS reacts with the hydroxyl groups on the SiO_2 surface, forming a siloxane-based compound. The non-polar methyl groups in this compound effectively isolate the substrate surface, transforming it from hydrophilic to hydrophobic.

D. Functionalization

A 5 mM 1-pyrenebutyric acid *N*-hydroxysuccinimide ester (PBASE, Aladdin, N134794-250 mg) solution was prepared by dissolving it in *N*,*N*-dimethylformamide (DMF, Aladdin). The prepared PBASE solution was added to the specified GFET array and incubated for 12 hours. During incubation, the evaporation of the solution was carefully monitored. After 12 hours, the devices were cleaned once with DMF and rinsed three times with deionized water to remove any impurities adsorbed on the graphene surface. Next, two regions were treated with a nucleic acid probe solution of hsa-miR-125b dissolved in 1× PBS at a concentration of 5 μM and a volume of 15 μL. Similarly, another two regions were treated with a nucleic acid aptamer solution of Aβ42. This incubation step lasted for 3 hours.

Table 1 Aptamer/probe synthesis sequence

Aptamer	5′–3′ sequence
hsa-miR-125b probe	TCACAAGTTAGGGTCTCAGGGA[25]
Aβ42 aptamer	AGTCTAGGATTCGGCGTGGGTTAATTTTTTGCTGCCTGTGGTGTTGGGGCGGGTGCG[26]

Afterward, the devices were repeatedly rinsed three times with PBS buffer to prevent physical adsorption of the nucleic acid aptamers on the graphene channel surface. Finally, the devices were sequentially incubated with amine-terminated polyethylene glycol (PEG, Aladdin, 10 kDa) and ethanolamine (ETA, Aladdin) each for 1 hour, followed by washing with 1× PBS buffer.

Results and discussion

The multi-target GFET sensor array is shown in Fig. 1(a), which is fabricated with the following steps: (a) metal electrode deposition; (b) graphene transfer and patterning; (c) hydrophobic treatment of the device surface; (d) independent functionalization with multiple distinct recognition elements. Metal electrodes were deposited on a 300 nm silicon oxide wafer using photolithography and electron beam evaporation. Four operational regions were designed on each device, with each region containing four GFET arrays. To isolate the different operational regions, a hydrophobic SiO_2 material was deposited between regions to prevent the flow of solutions during functionalization, ensuring that each region undergoes independent functionalization. The dimensions of each GFET graphene channel are 30 μm × 10 μm. Fig. 1(b) illustrates the functionalization and detection process. To achieve simultaneous and specific detection of multiple biological targets, two regions of the GFET array are treated with a hsa-miR-125b-specific complementary DNA capture probe, while another two regions are functionalized with an Aβ42-specific aptamer. Since graphene grown by chemical vapor deposition (CVD) cannot directly bond with aptamer/probe, PBASE was used as an intermediate linker.

The Aβ42 DNA aptamer and the hsa-miR-125b DNA probe were then functionalized in different regions. Amine-terminated polyethylene glycol (PEG, Aladdin, 10 kDa) is used during the functionalization process to increase the Debye length, thereby extending the concentration detection range. Finally, ethanolamine (ETA, Aladdin) is used as a blocking agent to reduce non-specific adsorption and enhance the sensitivity and specificity of target molecule detection.

Fig. 2 illustrate the surface wettability characterization of the GFET platform before and after HMDS treatment. When a droplet is placed on a solid surface, its equilibrium contact angle (θ) is governed by the balance of interfacial tensions at the three-phase boundary.[27,28] A smaller contact angle indicates a higher surface polarity and stronger liquid spreading, whereas a larger angle corresponds to enhanced hydrophobicity. The untreated SiO_2 surface, upon exposure to air, undergoes hydroxylation, forming hydroxyl (–OH) groups that increase surface polarity, resulting in a low contact angle (~44.0°), as shown in Fig. 2(a) and (b). After HMDS treatment, the hydroxyl groups are replaced by non-polar methyl groups, which reduce surface polarity and markedly enhance hydrophobicity. As shown in Fig. 2(c) and (d), this modification resulted in a contact angle of 83.7°, nearly doubling the original value, confirming the successful transformation of the surface from hydrophilic to hydrophobic.

Such surface engineering is crucial for confined liquid handling in biosensor applications, as it ensures spatial isolation of aptamer/probe-functionalized regions, thereby enhancing detection accuracy and reliability. The detailed derivation of Young's equation and the general reaction scheme of HMDS with surface hydroxyl groups are provided in the SI. In addition to the initial contact angle characterization shown in Fig. 2, the long-term stability and functional reliability of the HMDS modification were further examined. As demonstrated in Fig. S1, the hydrophobic surface remains stable even one month after treatment, confirming the robustness of the chemical modification. Furthermore, during the aptamer/probe functionalization process, which typically lasts for 3 h, the droplets maintained clear spatial separation without merging across different regions (Fig. S2). These results provide strong evidence that the HMDS treatment not only enhances hydrophobicity but also ensures reliable multi-target functionalization on the GFET platform.

Fig. 3(a) and (b) show the transfer curves of GFETs after each functionalization step for detecting hsa-miR-125b and Aβ42 targets, respectively. After PBASE immobilization, the Dirac point exhibits a rightward shift in both hsa-miR-125b and Aβ42 functionalized GFETs. This shift is attributed to the electron-withdrawing nature of the carbonyl group in PBASE, which induces electron transfer from the graphene surface to the PBASE molecule.

Table 2 Synthesis sequence of target biomarkers

Biomarker	Sequence
hsa-miR-125b sample	UCCCUGAGACCCUAACUUGUGA
Aβ42 sample	DAEFRHDSGYEVHHQKLVFFAEDVGSNKGAIIGLMVGGVVIA

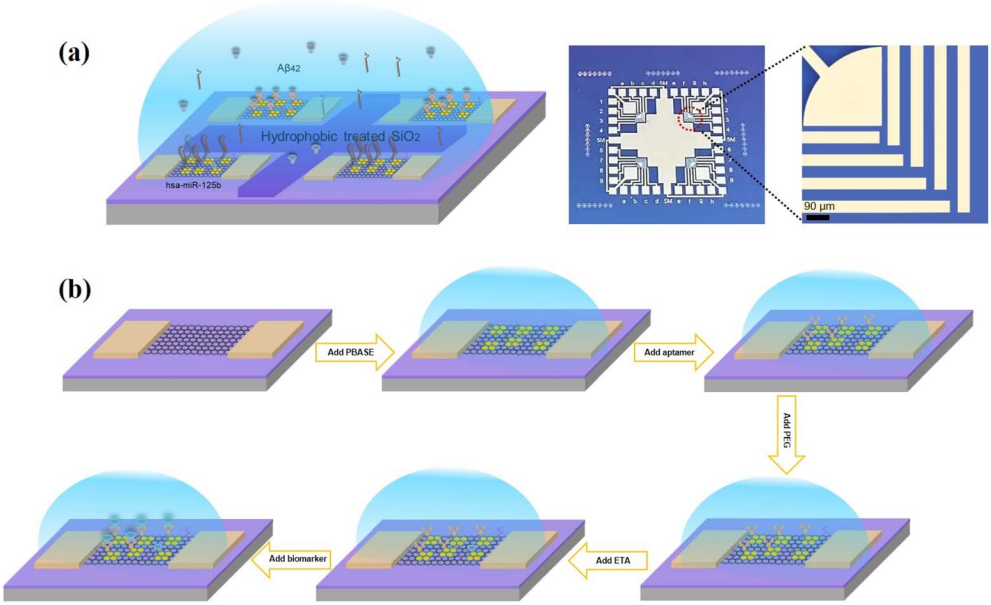

Fig. 1 (a) Schematic illustration representing a structure of a multi-target GFET biosensor. The right-hand optical micrograph shows the fabricated chip (overall size ≈ 1 cm × 1 cm) comprising four sensing regions, each containing four parallel GFET channels. The enlarged image highlights one representative sensing region, with the scale bar of 90 μm. (b) Functionalization process on graphene surface, including immobilizing PBASE, aptamer/probe, PEG, ETA and biomarker sequentially.

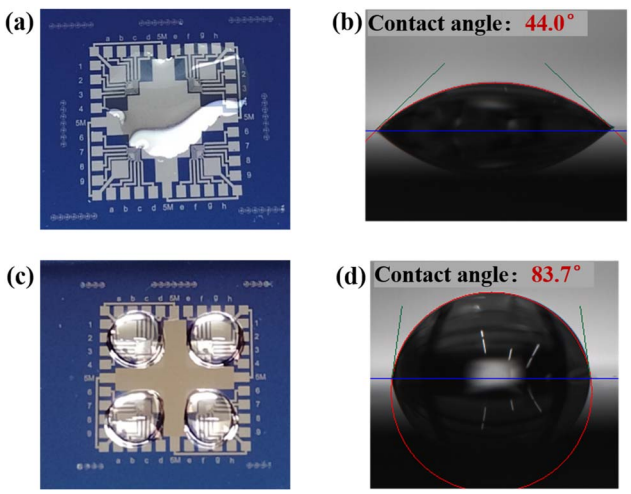

Fig. 2 (a) Device without hydrophobic treatment. (b) Contact angle of the device surface without hydrophobic treatment. (c) Device after hydrophobic treatment. (d) Contact angle of the device surface after hydrophobic treatment.

To further quantify the concentration-dependent sensing behavior, calibration analyses were performed based on the data shown in Fig. 3(c) and (d). As presented in Fig. 3(e) and (f), the Dirac-point voltage shift (ΔV_{cnp}) exhibits a nonlinear, saturation-type dependence on target concentration for both biomarkers, which is characteristic of affinity-based molecular binding processes. Accordingly, the calibration curves were fitted using a Hill-type binding model. Excellent agreement between the experimental data and the fitted curves was obtained, with correlation coefficients of $R^2 = 0.986$ for the hsa-miR-125b channel and $R^2 = 0.997$ for the Aβ42 channel, indicating high reproducibility and reliable concentration-dependent responses over the tested range.

It should be noted that, in this work, the sensing performance is evaluated based on differential electrical responses between spatially separated recognition regions on the same chip, where an orthogonal (non-cognate) channel serves as an internal reference. Under this measurement scheme, a conventional analytical limit of detection derived from PBS-only electrical noise (*e.g.*, the 3σ/slope method) is not directly applicable. Therefore, the term "LOD" in this study refers to the lowest tested concentration at which a statistically distinguishable differential ΔV_{cnp} response can be consistently resolved from the internal reference channel. Using this criterion, both hsa-miR-125b and Aβ42 biomarkers can be reliably detected down to 1 fM, as supported by consistent responses observed across $n \geq 13$ independent GFET devices.

The depletion of electron density increases hole concentration, leading to p-type doping, thereby shifting the Dirac voltage toward a higher gate voltage. Following further functionalization with aptamer molecules, the Dirac point undergoes a leftward shift. The negatively charged phosphate backbone of DNA aptamer/probe serves as an electron donor upon interaction with then-type doping, increasing the electron density in graphene and shifting the Dirac voltage toward a lower gate voltage. Upon target molecule binding, the Dirac point undergoes a further shift depending on the charge characteristics of the biomarker. hsa-miR-125b, as a negatively charged RNA molecule, introduces additional electrons, further shifting the Dirac point to the left due to enhanced n-type doping. Conversely, Aβ42, a peptide molecule containing polar groups

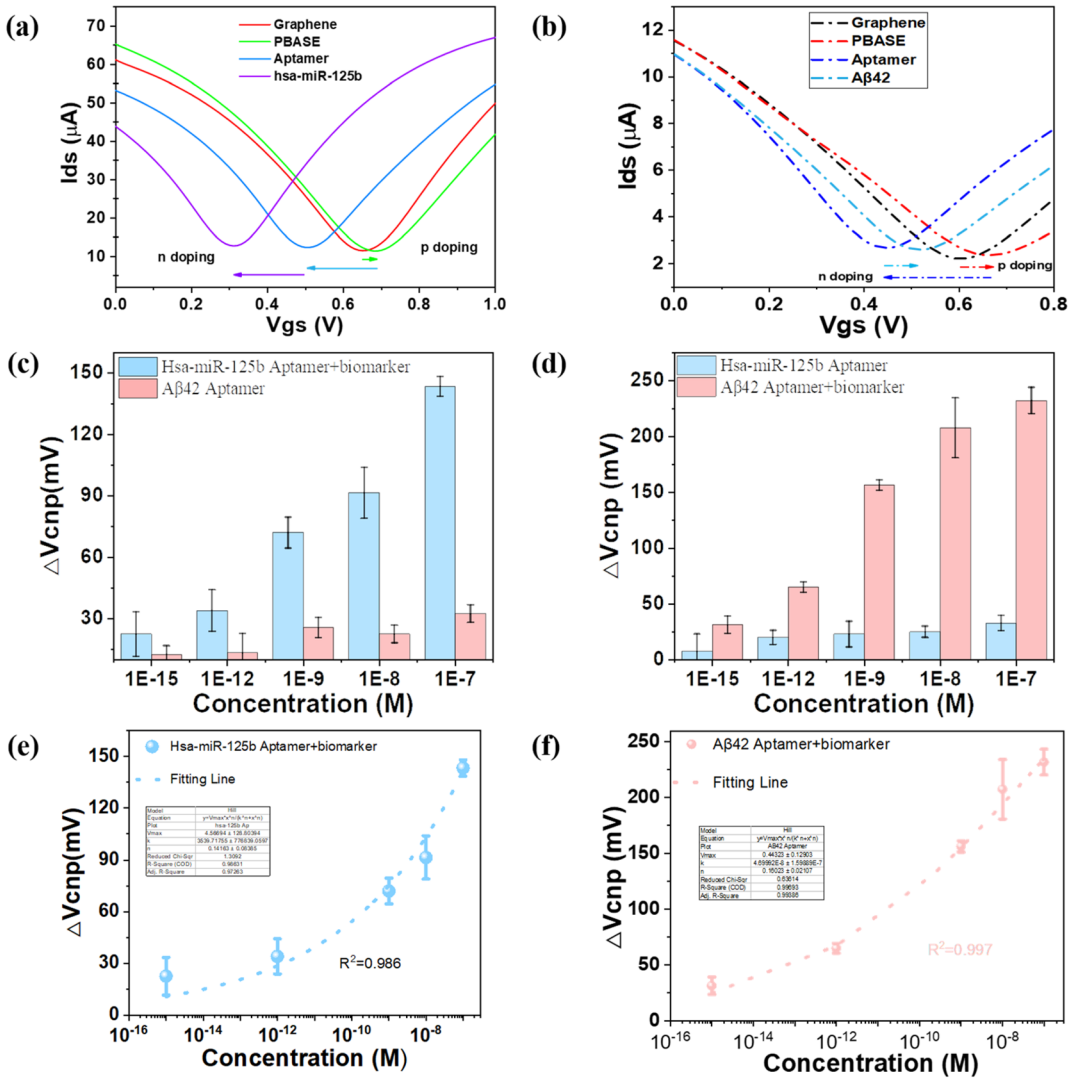

Fig. 3 The electrical sensing results of GFET biosensor. (a) (PBASE: 5 mM; aptamer: 5 μM). (b) GFET transfer curves for Aβ42 detection under identical functionalization. (c) Four regions functionalized with Aβ42 and hsa-miR-125b aptamers in 1× PBS, with Aβ42 target added for measuring the average signal response at different concentrations. (d) Four regions functionalized with Aβ42 and hsa-miR-125b aptamers in 1× PBS, with hsa-miR-125b target added for measuring the average signal response at different concentrations. (e) The sensor response as a function 125b concentration, with mean, standard deviation, median, and a linear fitting curve. (f) The sensor response as a function Aβ42 concentration, with mean, standard deviation, median, and a linear fitting curve ($n \geq 13$, n is number of sensors used for each measurement) ($n \geq 13$, n is number of sensors used for each measurement).

(such as amino and carboxyl groups), interacts with the aptamer/probe on the graphene surface through electrostatic or covalent bonding. This interaction can cause electron loss, generating holes and reducing the electron concentration, which forms p-type doping and shifts the Dirac point to the right. Such shifting of the *I–V* curves is consistent with previously reported results.[29–31]

To evaluate the sensitivity and detection range of the aptamer/probe-modified GFET biosensor, we investigated the sensor response by testing two different AD biomarkers, Aβ42 and hsa-miR-125b. We observed that the Dirac point voltage shift in the sensor array exhibited a significant positive correlation with the biomarker concentration ranging from 1 fM to 100 nM (Fig. 3(c) and (d)). Additionally, the non-specific binding signals were significantly lower than the specific signals. The results in Fig. 3(c) further confirm that the specific signal generated by the probe binding to their target molecules, which is based on base-pairing complementarity, significantly increases with the concentration of hsa-miR-125b, while the change in non-specific signals remains relatively small. Fig. 3(d) shows that the specific signal in the Aβ42 aptamer-modified graphene channel increases with the concentration of the sample solution. At a concentration of 1 fM, the signal change is minimal. In contrast, the ΔV_{cnp} change in the hsa-miR-125b probe-modified graphene channel is significantly lower, which corresponds to non-specific signals, and the non-specific signal data remain consistent across different concentrations. Statistical analysis using two-tailed Welch's *t*-tests demonstrated that

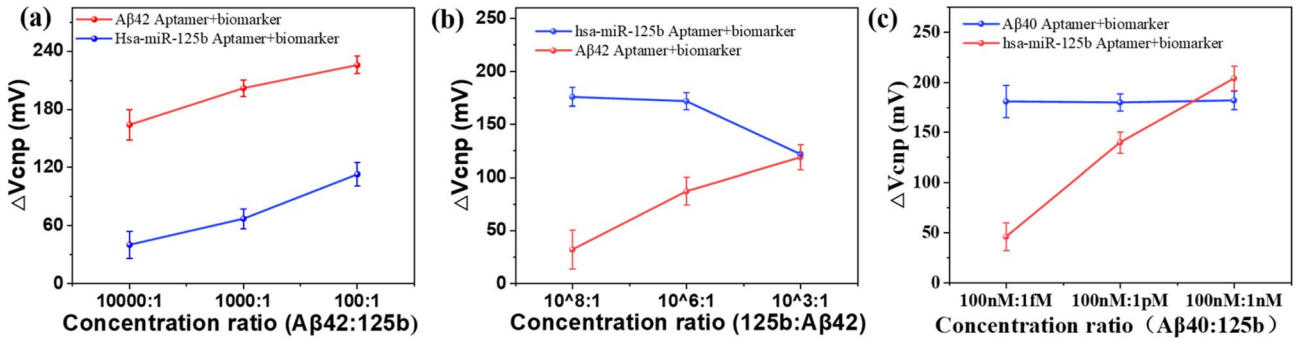

Fig. 4 Mixed sample detection results. (a) Higher concentration of Aβ42 biomarker *vs.* lower concentration of hsa-miR-125b biomarker. The absolute concentrations were (Aβ42 : 125b): 10 pM : 1 fM (10 000 : 1); 50 nM : 50 pM (1000 : 1); and 100 nM : 1 nM (100 : 1). (b) Higher concentration of hsa-miR-125b biomarker *vs.* lower concentration of Aβ42 biomarker. The absolute concentrations were (125b : Aβ42): 100 nM : 1 fM (10^8 : 1), 100 nM : 1 pM (10^6 : 1), and 50 nM : 50 pM (10^3 : 1). (c) Fixed concentration of Aβ40 biomarker and varying concentrations of hsa-miR-125b ($n \geq 13$, n is number of sensors used for each measurement).

the signal responses were significantly higher than the non-specific signals, confirming a reliable detection limit of 1 fM ($p < 0.05$). Detailed p-values are provided in Tables S1 and S2 of the SI.

The results demonstrate that the multi-target graphene transistor sensor chip exhibits high specificity and is capable of simultaneously detecting multiple biomolecules.

To demonstrate the multi-target sensing capability of the aptamer/probe-modified GFET biosensor array, we fabricated GFET arrays modified with specific aptamers for Aβ40, Aβ42, and hsa-miR-125b probe. These GFET arrays were exposed to sample solutions containing two different concentrations of mixed biomarker molecules. After introducing the mixed AD biomarkers, a significant ΔV_{cnp} change was observed only in the GFET devices containing specific recognition elements for the target AD biomarkers (Fig. 4(a)–(c)). As shown in Fig. 4(a)–(c), different responses were generated when various recognition-elements were modified onto different regions of the same chip, in response to the mixed sample solution containing multiple biomarkers. Specifically, high-concentration samples exhibited larger response signals, while low-concentration samples showed smaller responses. As the concentration of the two biomarker molecules increased, the response signals also increased, which is consistent with the experimental results for single-molecule detection. This demonstrates that the sensor chip can detect changes in the concentration of a single biomarker molecule in complex samples. The stronger response signals from the higher-concentration biomolecules in the mixed solution are an expected phenomenon, further confirming that the sensor chip can simultaneously recognize and detect two different biomarker molecules.

Conclusions

In summary, this study successfully developed a GFET-based multiplexed sensing platform modified with aptamer/probe. Through hydrophobization of the blocking layer material, the platform is capable of simultaneously and specifically detecting multiple AD biomarkers, with the lowest tested concentration of 1 fM. Compared to existing technologies, this platform offers broader applicability, ease of operation, and high sensitivity at low concentration ranges. Notably, this platform significantly enhances diagnostic efficiency without compromising detection quality, providing an innovative solute on for the early screening of AD and the dynamic monitoring of biomarker concentration changes. This technology opens new avenues for multiplexed, label-free electrical detection of AD-related biomarkers and provides a promising proof-of-concept for future precision-diagnosis platforms. Further validation in clinically relevant biological matrices will be pursued in subsequent studies.

Author contributions

Biyu Guo: investigation (equal); methodology (equal); writing – original draft (equal); writing review & editing (equal). Jiangyang Wang: writing – original draft (equal); writing review & editing (equal). Feige Lou: writing – review & editing (equal). Baowei Yuan: writing – review & editing (equal). Zhibo Chen: writing – review & editing (equal). Chengjie Tang: writing – review & editing (equal). Weiao Chen: writing – review & editing (equal). Fangxuan Yi: writing – review & editing (equal). Jingjing Jiang: writing – review & editing (equal). Guangxi Hu: writing – review & editing (equal). Yiqiang Zhan: writing – review & editing (equal). Ye Lu: funding acquisition (equal); conceptualization (equal); methodology (equal); project administration (equal); supervision (equal); writing – original draft (equal); writing – review & editing (equal).

Conflicts of interest

The authors declare no conflict of interest.

Data availability

The data that support the findings of this study are available from the corresponding author upon reasonable request.

Supplementary information (SI) is available. See DOI: https://doi.org/10.1039/d5ra07384g.

Acknowledgements

This work was supported in part by National Key Research and Development Program (Grant No. 2021YFA-1200500). Natural Science Foundation of China (Grant No. 62374034, 62350610270). Innovation Program of Shanghai Municipal Education Commission (Grant No. 2021-01-07-00-07-E00077) and Natural Science Foundation of Shanghai (Grant No. 22ZR1403500, 24JD1401000, 24JD1400600) and Lingang Laboratory (Grant No. LGL8998-01).

References

1 F. Wei, P. Patel, W. Liao, *et al.*, Electrochemical Sensor for Multiplex Biomarkers Detection, *Clin. Cancer Res.*, 2009, **15**(13), 4446–4452.
2 P. Samadi Pakchin, F. Fathi, H. Samadi and K. Adibkia, Recent advances in receptor-based optical biosensors for the detection of multiplex biomarkers, *Talanta*, 2025, **281**, 126852.
3 J. U. Lee, A. H. Nguyen and S. J. Sim, A nanoplasmonic biosensor for label-free multiplex detection of cancer biomarkers, *Biosens. Bioelectron.*, 2015, **74**, 341–346.
4 L. Lu, W. Z. Dai, X. C. Zhu and T. Ma, Analysis of Serum miRNAs in Alzheimer's Disease, *Am. J. Alzheimer's Dis. Other Dementias*, 2021, **36**, 15333175211021712.
5 X. Duan, Q. Zheng, L. Liang and L. Zhou, Serum Exosomal miRNA-125b and miRNA-451a are Potential Diagnostic Biomarker for Alzheimer's Diseases, *Degener. Neurol. Neuromuscular Dis.*, 2024, **14**, 21–31.
6 J. Pannee, E. Portelius, L. Minthon, *et al.*, Reference measurement procedure for CSF amyloid beta (Aβ) 1–42 and the CSF Aβ1–42/Aβ1–40 ratio–a cross-validation study against amyloid PET, *J. Neurochem.*, 2016, **139**(4), 651–658.
7 M. Amft, M. Ortner, U. Eichenlaub, *et al.*, The cerebrospinal fluid biomarker ratio Aβ42/40 identifies amyloid positron emission tomography positivity better than Aβ42 alone in a heterogeneous memory clinic cohort, *Alzheimer's Res. Ther.*, 2022, **14**(1), 60.
8 Z. Dong, H. Gu, Q. Guo, *et al.*, Profiling of Serum Exosome MiRNA Reveals the Potential of a MiRNA Panel as Diagnostic Biomarker for Alzheimer's Disease, *Mol. Neurobiol.*, 2021, **58**(7), 3084–3094.
9 M. Hueso, R. Griñán, A. Mallen, *et al.*, MiR-125b downregulates macrophage scavenger receptor type B1 and reverse cholesterol transport, *Biomed. Pharmacother.*, 2022, **146**, 112596.
10 S. J. Teipel, M. Grothe, S. Lista, *et al.*, Relevance of Magnetic Resonance Imaging for Early Detection and Diagnosis of Alzheimer Disease, *Med. Clin. North Am.*, 2013, **97**(3), 399–424.
11 I. D. de Souza and M. E. C. Queiroz, Advances in sample preparation and HPLC–MS/MS methods for determining amyloid-β peptide in biological samples: a review, *Anal. Bioanal. Chem.*, 2023, **415**(18), 4003–4021.
12 D. Chiasserini, L. Biscetti, L. Farotti, *et al.*, Performance Evaluation of an Automated ELISA System for Alzheimer's Disease Detection in Clinical Routine, *J. Alzheimer's Dis.*, 2016, **54**(1), 55–67.
13 A. D. Cohen and W. E. Klunk, Early detection of Alzheimer's disease using PiB and FDG PET, *Neurobiol. Dis.*, 2014, **72**, 117–122.
14 J. H. Kang, H. Vanderstichele, J. Q. Trojanowski and L. M. Shaw, Simultaneous analysis of cerebrospinal fluid biomarkers using microsphere-based xMAP multiplex technology for early detection of Alzheimer's disease, *Methods*, 2012, **56**(4), 484–493.
15 C. Li, Y. Yang, S. Luo, *et al.*, GNG5 is a novel regulator of Aβ42 production in Alzheimer's disease, *Cell Death Dis.*, 2024, **15**(11), 815.
16 M. Rice, G. J. Nuovo, D. Sawant, *et al.*, Comparison of Neuroinflammation Induced by Hyperphosphorylated Tau Protein Versus Ab42 in Alzheimer's Disease, *Mol. Neurobiol.*, 2024, **61**(7), 4589–4601.
17 M. Polak, J. Wieczorek, M. Botor, *et al.*, Principles and limitations of miRNA purification and analysis in whole blood collected during ablation procedure from patients with atrial fibrillation, *J. Clin. Med.*, 2024, **13**(7), 1898.
18 K. Wright, K. de Silva, A. C. Purdie, *et al.*, Comparison of methods for miRNA isolation and quantification from ovine plasma, *Sci. Rep.*, 2020, **10**(1), 825.
19 A. Keshavan, H. Wellington, Z. Chen, *et al.*, Concordance of CSF measures of Alzheimer's pathology with amyloid PET status in a preclinical cohort: a comparison of Lumipulse and established immunoassays, *Alzheimer's & Dementia: Diagnosis, Assessment & Disease Monitoring*, 2021, **13**(1), e12131.
20 M. Donnelly, D. Mao, J. Park and G. Xu, Graphene field-effect transistors: the road to bioelectronics, *J. Phys. D Appl. Phys.*, 2018, **51**(49), 493001.
21 M. Sun, S. Wang, Y. Liang, *et al.*, Flexible Graphene Field-Effect Transistors and Their Application in Flexible Biomedical Sensing, *Nano-Micro Lett.*, 2025, **17**(1), 34.
22 M. Sun, S. Wang, Y. Zhang, *et al.*, An Ultrasensitive Flexible Biosensor Enabled by High-Performance Graphene Field-Effect Transistors with Defect-Free van der Waals Contacts for Breast Cancer miRNA Fast Detection, *Talanta*, 2025, **287**, 127637.
23 J. Gao, C. Wang, Y. Chu, *et al.*, Graphene Oxide–Graphene van der Waals Heterostructure Transistor Biosensor for SARS-CoV-2 Protein Detection, *Talanta*, 2022, **240**, 123197.
24 J. Gao, C. Wang, C. Wang, *et al.*, Poly-L-lysine-Modified Graphene Field-Effect Transistor Biosensors for Ultrasensitive Breast Cancer miRNAs and SARS-CoV-2 RNA Detection, *Anal. Chem.*, 2022, **94**(3), 1626–1636.
25 M. Salehirozveh, P. Dehghani, M. Zimmermann, V. A. L. Roy and H. Heidari, Graphene Field Effect Transistor Biosensors Based on Aptamer for Amyloid- β Detection, *IEEE Sens. J.*, 2020, **20**(21), 12488–12494.

26 J. Chen, Y. Chen and Z. Chen, miR-125a/b Regulates the Activation of Cancer Stem Cells in Paclitaxel-resistant Colon Cancer, *Cancer Invest.*, 2013, **31**(1), 17–23.
27 T. Young, An Essay on the Cohesion of Fluids, *Philos. Trans. R. Soc. London*, 1805, **95**, 65–87.
28 S. Parvate, P. Dixit and S. Chattopadhyay, Superhydrophobic Surfaces: Insights from Theory and Experiment, *J. Phys. Chem. B*, 2020, **124**(8), 1323–1360.
29 A. K. Jahromi, *et al.*, Experimental Comparison of Direct and Indirect Aptamer-Based Biochemical Functionalization of Electrolyte-Gated Graphene Field-Effect Transistors for Biosensing Applications, *Anal. Chim. Acta*, 2022, **1222**, 340177.
30 K. E. Laliberte, *et al.*, A Wearable Graphene Transistor-Based Biosensor for Monitoring IL-6 Biomarker, *Microelectron. Eng.*, 2022, **262**, 111835.
31 X. Wang, *et al.*, Measurements of Aptamer–Protein Binding Kinetics Using Graphene Field-Effect Transistors, *Nanoscale*, 2019, **11**(26), 12573–12581.